# Cooper pairing, flat-band superconductivity, and quantum geometry in the pyrochlore-Hubbard model

M. Iskin
*Department of Physics, Koç University, Rumelifeneri Yolu, 34450 Sarıyer, Istanbul, Türkiye*

(Received 7 March 2024; accepted 22 April 2024; published 3 May 2024)

We investigate the impacts of the quantum geometry of Bloch states, specifically through the band-resolved quantum-metric tensor, on Cooper pairing and flat-band superconductivity in a three-dimensional pyrochlore-Hubbard model. First we analyze the low-lying two-body spectrum exactly, and show that the pairing order parameter is uniform in this four-band lattice. This allows us to establish direct relations between the superfluid weight of a multiband superconductor and (i) the effective mass of the lowest-lying two-body branch at zero temperature, (ii) the kinetic coefficient of the Ginzburg-Landau theory in proximity to the critical temperature, and (iii) the velocity of the low-energy Goldstone modes at zero temperature. Furthermore, we perform a comprehensive numerical analysis of the superfluid weight and Goldstone modes, exploring both their conventional and geometric components at zero temperature.

DOI: 10.1103/PhysRevB.109.174508

## I. INTRODUCTION

The complex quantum geometric tensor serves as a central and defining concept in modern solid-state and condensed-matter physics [1–3]. Its imaginary component is in the form of an antisymmetric tensor known as the Berry curvature, and the associated Chern number has proven instrumental in the classification of topological insulators and superconductors [4–7]. Its real part is in the form of a symmetric tensor known as the quantum metric, and it quantifies the quantum distance between adjacent Bloch states. Despite a long history of interdisciplinary interest in various physical phenomena governed by the Berry curvature, nature has been less forthcoming regarding the effects of the quantum metric. Only in the past decade or so have researchers increasingly recognized the significance of the quantum metric in various contexts. Notably, following the pioneering work by Peotta and Törmä in 2015 on the origins of superfluidity in topologically nontrivial flat bands [8], a deeper connection between the transport properties of a multiband superconductor and the quantum geometry of its Bloch states has emerged as a surprising revelation in recent years [9–14].

Theoretical interest in flat-band superconductivity dates back a long time, as materials hosting quasiflat Bloch bands were envisioned as a potential pathway to achieve room-temperature superconductivity [15,16]. This anticipation was grounded in the naive BCS theory, which was suggested by the relatively elevated single-particle density of states within narrower Bloch bands. However, it is crucial to emphasize that the microscopic mechanism underpinning the emergence of flat-band superconductivity was completely absent in these earlier studies. It remained unclear whether superconductivity could thrive within an isolated flat band, given that the infinite effective band mass hampers the potential for localized particles on the lattice to attain superconductivity, thus acting as an inhibiting factor. As a result, it was believed that superconductivity was strictly prohibited when the permissible Bloch states originated solely from a single flat band [17].

Recent studies illuminated these two perplexing arguments and unveiled a physical mechanism that theoretically permits the existence of flat-band superconductors [9–11]. It has been demonstrated that multiband lattices (such as in moiré materials) contribute differently to the superfluid weight. The real intraband processes were associated with the conventional contribution, while the virtual interband processes were linked to the geometric aspect. Unlike the conventional contribution [18,19], which is solely determined by the derivatives of the Bloch bands, the geometric contribution is also influenced by the derivatives of the associated Bloch states. Consequently, unless the geometric contribution is nullified, superconductivity can manifest within a flat band, thanks to the involvement of other flat or dispersive bands through interband processes. There are also alternative proposals involving two-band systems as a potential means to achieve high-critical temperatures in the BCS-BEC crossover. [20,21].

These findings highlight the necessity of considering not only the dispersion of the Bloch bands, but also the geometry of the Bloch states in the pursuit of high-critical-temperature superconductivity. It is only by incorporating both factors that we can fully exploit their potential. A nontrivial quantum geometry is indispensable, as the mere presence of a flat band does not guarantee superconductivity if its geometry is trivial. Thus, the emerging field of quantum geometry within multiband superconductors holds substantial potential for advancing our understanding of flat-band superconductors, assuming Hubbard-type tight-binding Hamiltonians mimic their underlying low-energy physics. Despite the significant progress made with one-dimensional and two-dimensional lattices that feature flat bands [9,10,22–33], there has been limited exploration of more realistic three-dimensional lattices due to the technical complexities and challenges associated with their analysis. Our aim is to

 

fill this gap by investigating quantum-geometric effects in a pyrochlore-Hubbard model, where the pyrochlore lattice consists of a three-dimensional arrangement of tetrahedra sharing corners, possesses cubic symmetry, and is commonly encountered in transition-metal and rare-earth oxide materials, especially in oxide compounds [34]. Given the recent demonstrations of three-dimensional flat bands and superconductivity in a pyrochlore metal $CaNi_2$ [35] and pyrochlore superconductor $CeRu_2$ [36], these structures present a compelling lattice platform for exploring the interplay between quantum geometry and strong correlations.

The rest of the paper is organized as follows. In Sec. II, we introduce the pyrochlore lattice and discuss its one-body spectrum. In Sec. III, we calculate the low-lying two-body spectrum for the pyrochlore-Hubbard model and derive the effective mass tensor of the lowest-lying branch. In Sec. IV, we analyze the superfluid weight at zero and finite temperatures, relate it to the velocity of the low-energy Goldstone modes at zero temperature, and present their thorough numerical exploration in Sec. V. The paper ends with a summary and an outlook in Sec. VI, and the Gaussian fluctuations and numerical implementations are discussed in Appendixes A and B.

## II. ONE-BODY PROBLEM

The pyrochlore lattice is one of the simplest three-dimensional tight-binding models that feature a flat band in the Bloch spectrum [37,38]. It has an underlying face-centered-cubic Bravais lattice that can be defined by the primitive unit vectors $\mathbf{a}_1 = (0, a/2, a/2)$, $\mathbf{a}_2 = (a/2, 0, a/2)$, and $\mathbf{a}_3 = (a/2, a/2, 0)$, where $a$ is the side length of the conventional simple-cubic cell. Its basis consists of $N_S = 4$ sublattice sites that are located at $\mathbf{r}_A = (0, 0, 0)$, $\mathbf{r}_B = \mathbf{a}_1/2$, $\mathbf{r}_C = \mathbf{a}_2/2$, and $\mathbf{r}_D = \mathbf{a}_3/2$. The corresponding first Brillouin zone (BZ) has the shape of a truncated octahedron with a side length $\sqrt{2}\pi/a$. The associated reciprocal space is such that $\sum_{\mathbf{k}\in \mathrm{BZ}} 1 = N_c$, where $\mathbf{k} = (k_x, k_y, k_z)$ is the crystal momentum in units of $\hbar \to 1$ and $N_c$ is the number of unit cells in the system. That is, the total volume of the system is $\mathcal{V} = N_c a^3/4$, where $32\pi^3/a^3$ is the volume of the BZ in reciprocal space, $a^3/4$ is the volume of the primitive cell in real space, and $N = 4N_c$ is the total number of lattice sites in the system.

Having a spin-1/2 system in mind with $\sigma = \{\uparrow, \downarrow\}$ labeling the spin projections, the Bloch Hamiltonian for such a lattice can be written as $\mathcal{H}_0 = \sum_{SS'\sigma\mathbf{k}} h^{\mathbf{k}}_{SS'} c^\dagger_{S\mathbf{k}\sigma} c_{S'\mathbf{k}\sigma}$, where $c_{S\mathbf{k}\sigma}$ annihilates a spin-$\sigma$ particle on the sublattice $S \equiv \{A, B, C, D\}$ with momentum $\mathbf{k}$. The elements $h^{\mathbf{k}}_{SS'} = h^{\mathbf{k}}_{S'S}$ of the Hamiltonian matrix $\mathbf{h}_{\mathbf{k}}$ are real such that $h^{\mathbf{k}}_{SS} = 0$, $h^{\mathbf{k}}_{AB} = -2\bar{t}\cos(\frac{k_y+k_z}{4}a)$, $h^{\mathbf{k}}_{AC} = -2\bar{t}\cos(\frac{k_x+k_z}{4}a)$, $h^{\mathbf{k}}_{AD} = -2\bar{t}\cos(\frac{k_x+k_y}{4}a)$, $h^{\mathbf{k}}_{BC} = -2\bar{t}\cos(\frac{k_x-k_y}{4}a)$, $h^{\mathbf{k}}_{BD} = -2\bar{t}\cos(\frac{k_x-k_z}{4}a)$, and $h^{\mathbf{k}}_{CD} = -2\bar{t}\cos(\frac{k_y-k_z}{4}a)$, where $\bar{t}$ is the hopping parameter between the nearest-neighbor sites. Thus, $h^{\mathbf{k}}_{SS'} = (h^{-\mathbf{k}}_{SS'})^*$ respects time-reversal symmetry. The resultant eigenvalue problem, i.e.,

$$\sum_{S'} h^{\mathbf{k}}_{SS'} n_{S'\mathbf{k}} = \varepsilon_{n\mathbf{k}} n_{S\mathbf{k}}, \tag{1}$$

leads to four Bloch bands in the one-body spectrum, where $\varepsilon_{1\mathbf{k}} = -2\bar{t}(1+\sqrt{1+\Lambda_{\mathbf{k}}})$ and $\varepsilon_{2\mathbf{k}} = -2\bar{t}(1-\sqrt{1+\Lambda_{\mathbf{k}}})$ are the dispersive bands with $\Lambda_{\mathbf{k}} = \cos(k_x a/2)\cos(k_y a/2) + \cos(k_y a/2)\cos(k_z a/2) + \cos(k_x a/2)\cos(k_z a/2)$, and $\varepsilon_{3\mathbf{k}} = \varepsilon_{4\mathbf{k}} = 2\bar{t}$ are the flat bands. These bands are sketched in Fig. 1(a) along the high-symmetry points. In this paper, since we prefer the flat bands to appear at the bottom of the spectrum, we set $\bar{t} \to -t$ and choose $t > 0$ as the unit of energy.

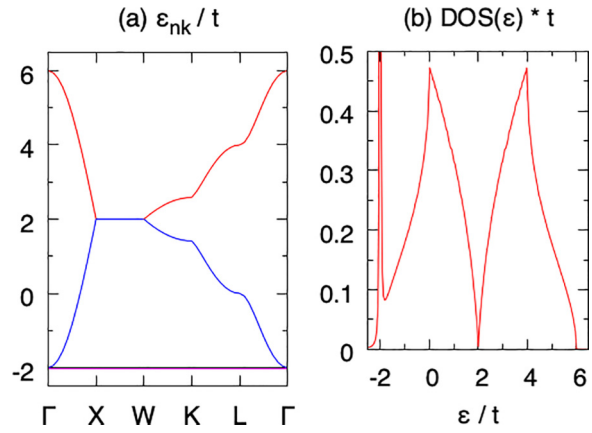


FIG. 1. (a) Bloch bands are shown along the high-symmetry points in the first BZ where $\Gamma \equiv (0, 0, 0)$, $X \equiv (0, 0, 2\pi/a)$, $W \equiv (\pi/a, 0, 2\pi/a)$, $K \equiv (\pi/2a, \pi/2a, 2\pi/a)$, and $L \equiv (\pi/a, \pi/a, \pi/a)$. (b) Density of states per unit cell per spin as a function of energy.

In Fig. 1(b), we also show the single-particle density of states per unit cell per spin, $\mathrm{DOS}(\varepsilon) = \frac{1}{N_c}\sum_{n\mathbf{k}} \delta(\varepsilon - \varepsilon_{n\mathbf{k}})$, where the Dirac $\delta$ function is represented via a Lorentzian distribution $\delta(x) = \frac{1}{\pi}\lim_{\eta\to 0}\frac{\eta}{x^2+\eta^2}$ with $\eta = 0.001t$. This is the origin of the energy broadening around $\varepsilon = -2t$. The van Hove singularities are clearly visible at $\varepsilon = \{0, 4t\}$, and the density of states vanishes linearly at $\varepsilon = 2t$ with logarithmic corrections in its vicinity. The total bandwidth is $8t$.

## III. TWO-BODY PROBLEM

In this paper, we consider the simplest Hubbard model with an on-site attractive interaction between an $\uparrow$ and a $\downarrow$ particle,

$$\mathcal{H} = \mathcal{H}_0 - \frac{U}{N_c}\sum_{S\mathbf{k}\mathbf{k}'\mathbf{q}} c^\dagger_{S\mathbf{k}\uparrow} c^\dagger_{S,-\mathbf{k}+\mathbf{q},\downarrow} c_{S,-\mathbf{k}'+\mathbf{q},\downarrow} c_{S\mathbf{k}'\uparrow}, \tag{2}$$

where $U \geqslant 0$. The two-body problem can be solved exactly through a variational approach [39], leading to a number of spin-singlet bound states for a given center-of-mass momentum $\mathbf{q}$. It turns out the low-lying two-body spectrum $E_{\ell\mathbf{q}}$ can be determined by $\mathbf{G}_{\mathbf{q}}\boldsymbol{\beta}_{\ell\mathbf{q}} = 0$, where $\mathbf{G}_{\mathbf{q}}$ is a $4\times 4$ Hermitian matrix with the following elements:

$$G^{\mathbf{q}}_{SS'} = \delta_{SS'} - \frac{U}{N_c}\sum_{nm\mathbf{k}} \frac{m^*_{S,\mathbf{k}-\mathbf{q}} n_{S\mathbf{k}} n^*_{S'\mathbf{k}} m_{S',\mathbf{k}-\mathbf{q}}}{\varepsilon_{n\mathbf{k}} + \varepsilon_{m,\mathbf{k}-\mathbf{q}} - E_{\ell\mathbf{q}}}. \tag{3}$$

Here, $\delta_{ij}$ is a Kronecker delta and we assumed time-reversal symmetry $\varepsilon_{n,-\mathbf{k}\downarrow} = \varepsilon_{n\mathbf{k}\uparrow} = \varepsilon_{n\mathbf{k}}$ and $n^*_{S,-\mathbf{k}\downarrow} = n_{S\mathbf{k}\uparrow} = n_{S\mathbf{k}}$, where $n_{S\mathbf{k}}$ is the sublattice projection $\langle S|n_{\mathbf{k}}\rangle$ of the periodic part $|n_{\mathbf{k}}\rangle$ of the Bloch state that is associated with $\varepsilon_{n\mathbf{k}}$ through Eq. (1). This yields a self-consistency relation for a given $E_{\ell\mathbf{q}}$, and its solutions can be found by setting the eigenvalues of $\mathbf{G}_{\mathbf{q}}$ to 0 one at a time. The corresponding

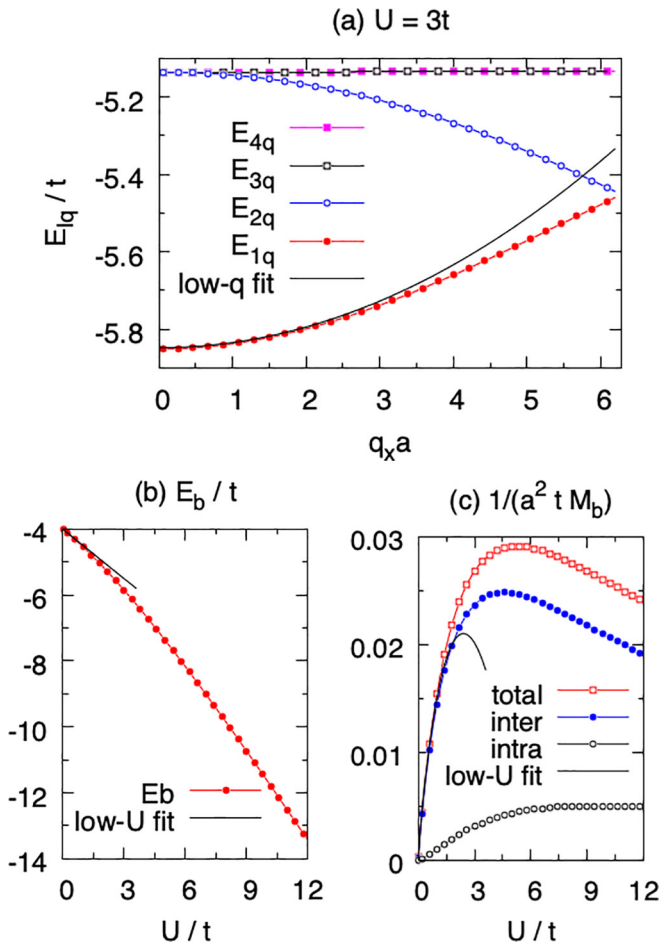


FIG. 2. (a) Spectrum $E_{\ell\mathbf{q}}$ of the low-lying bound states for $U = 3t$ as a function of $q_x$, when $q_y = 0$. The quadratic expansion $E_{1\mathbf{q}} = E_b + q_x^2/(2M_b)$ is an excellent fit for the lowest branch in the small-$q_x$ region. (b) Energy offset $E_{1\mathbf{0}}$ as a function of $U$. (c) Effective isotropic mass $1/M_b = 1/M_b^{\text{intra}} + 1/M_b^{\text{inter}}$ as a function of $U$ along with its intraband and interband contributions. The low-$U$ fit $1/(a^2 t M_b) \approx 0.028(U/t) - 0.013(U/t)^{1.45}$ is discussed in the text.

eigenvectors $\boldsymbol{\beta}_{\ell\mathbf{q}} = (\beta_{A\ell\mathbf{q}}, \beta_{B\ell\mathbf{q}}, \beta_{C\ell\mathbf{q}}, \beta_{D\ell\mathbf{q}})^{\mathrm{T}}$ can be used to characterize some physical properties of the bound states, where $T$ is the transpose. Thus, for a given $\mathbf{q}$, there are four bound states below the threshold $-4t$ of the lowest two-body continuum, and we label them with $\ell = \{1, 2, 3, 4\}$, starting with the lowest branch. These solutions are illustrated in Fig. 2(a) for $U = 3t$, where the degenerate branches $E_{3\mathbf{q}} = E_{4\mathbf{q}}$ appear almost flat in the shown scale since their bandwidths are roughly $0.002t$. The overall structure of the two-body spectrum is reminiscent of the underlying Bloch spectrum, but with the opposite sign of energy. Compare with the $\Gamma$ - $X$ portion in Fig. 1(a). This can be best understood in the $U/t \to \infty$, where the effective nearest-neighbor hopping parameter $t_p = 2t^2/U > 0$ for a strongly bound pair of $\uparrow$ and $\downarrow$ particles has the opposite sign compared to $\bar{t} < 0$ of its unpaired constituents. This is because when a bound state breaks up at a cost of binding energy $U$ in the denominator and its $\uparrow$ constituent hops to a neighboring site, the $\downarrow$ partner follows it and hops to the same site, leading to $\bar{t}_\uparrow \bar{t}_\downarrow = t^2$ in the numerator. The prefactor accounts for the possibility of change in the order of spins. Such a virtual dissociation is the only physical mechanism for a strongly bound pair of particles to move in the Hubbard model with nearest-neighbor hoppings.

Our numerical calculations also reveal that the so-called uniform-pairing condition [39], i.e., $\boldsymbol{\beta}_{1\mathbf{q}} \propto (1, 1, 1, 1)^{\mathrm{T}}$, is satisfied at all $U \neq 0$ for the lowest-lying $\ell = 1$ branch in the $\mathbf{q} \to \mathbf{0}$ limit. This finding suggests that the sublattice sites of a pyrochlore lattice in a unit cell must be equivalent by symmetry and make equal contribution to pairing. Thus, similar to the well-known two-dimensional toy models such as the Mielke-checkerboard and kagome lattices that exhibit uniform pairing, the pyrochlore lattice offers an ideal playground for theoretical studies on flat-band superconductivity in three dimensions. For instance, when the uniform-pairing condition is met together with the underlying time-reversal symmetry, the energy $E_{1\mathbf{q}}$ of the corresponding small-$\mathbf{q}$ bound states can be extracted simply from $\sum_{SS'} G^{\mathbf{q}}_{SS'} = 0$. In particular, it is possible to show that

$$E_{1\mathbf{q}} = E_b + \frac{1}{2}\sum_{ij}(M_b^{-1})_{ij} q_i q_j, \tag{4}$$

where the $\mathbf{q} = \mathbf{0}$ energy offset $E_b$ is determined by the self-consistency relation [39]

$$1 = \frac{U}{N}\sum_{n\mathbf{k}} \frac{1}{2\varepsilon_{n\mathbf{k}} - E_b}. \tag{5}$$

Furthermore, we split the elements of the inverse effective-mass tensor as $(M_b^{-1})_{ij} = (M_{\text{intra}}^{-1})_{ij} + (M_{\text{inter}}^{-1})_{ij}$, depending on whether the intraband or interband processes are involved, leading to [39]

$$\left(M_{\text{intra}}^{-1}\right)_{ij} = \frac{\sum_{n\mathbf{k}} \frac{\ddot{\varepsilon}^{ij}_{n\mathbf{k}}}{(2\varepsilon_{n\mathbf{k}} - E_b)^2}}{2\sum_{n\mathbf{k}} \frac{1}{(2\varepsilon_{n\mathbf{k}} - E_b)^2}}, \tag{6}$$

$$\left(M_{\text{inter}}^{-1}\right)_{ij} = \frac{\sum_{n\mathbf{k}} \frac{g^{n\mathbf{k}}_{ij}}{2\varepsilon_{n\mathbf{k}} - E_b} - \sum_{n,m\neq n,\mathbf{k}} \frac{g^{nm\mathbf{k}}_{ij}}{\varepsilon_{n\mathbf{k}} + \varepsilon_{m\mathbf{k}} - E_b}}{\sum_{n\mathbf{k}} \frac{1}{(2\varepsilon_{n\mathbf{k}} - E_b)^2}}. \tag{7}$$

Here the intraband contribution depends only on the derivatives of the Bloch spectrum, $\ddot{\varepsilon}^{ij}_{n\mathbf{k}} = \frac{\partial^2 \varepsilon_{n\mathbf{k}}}{\partial k_i \partial k_j}$, but the interband contribution also depends on the derivatives of the associated Bloch states through the elements of the so-called band-resolved quantum-metric tensor,

$$g^{nm\mathbf{k}}_{ij} = 2\mathrm{Re}\langle \dot{n}^i_{\mathbf{k}} | m_{\mathbf{k}} \rangle \langle m_{\mathbf{k}} | \dot{n}^j_{\mathbf{k}} \rangle, \tag{8}$$

where Re denotes the real part and $|\dot{n}^i_{\mathbf{k}}\rangle = \partial |n_{\mathbf{k}}\rangle / \partial k_i$. As the naming suggests, the elements of the quantum-metric tensor of the $n$th Bloch band [3] can be written as $g^{n\mathbf{k}}_{ij} = \sum_{m\neq n} g^{nm\mathbf{k}}_{ij}$. Their origin can be traced back to the power-series expansion of

$$|\langle n_{\mathbf{k}} | m_{\mathbf{k}-\mathbf{q}} \rangle|^2 = \delta_{nm} - \frac{1}{2}\sum_{ij}\left[g^{n\mathbf{k}}_{ij}\delta_{nm} + g^{nm\mathbf{k}}_{ij}(\delta_{nm} - 1)\right] q_i q_j \tag{9}$$

in the small-$\mathbf{q}$ limit.

In Figs. 2(b) and 2(c), we present the self-consistent solutions of Eqs. (5)–(7) for the pyrochlore lattice, where

the effective mass is isotropic in space. As an illustration, we show in Fig. 2(a) that the resultant $E_b \approx -5.8481t$ and $M_b \approx 37.3026/(a^2t)$ provide a perfect fit when $U = 3t$. Furthermore, in the $U/t \to 0$ limit when $E_b = -4t - U/2$, one can make analytical arguments that are based on some controlled approximations that $1/(a^2tM_b) \approx \tilde{A}_1(U/t) - \tilde{A}_2(U/t)^{\tilde{A}_3} \gg 1/(a^2tM_b^{\text{intra}})$ to the leading order, where $\tilde{A}_1$ and $\tilde{A}_2$ are numerical factors and $\tilde{A}_3 = 3/2$. Our numerical fit for $U/t \leqslant 0.1$ shows that $\tilde{A}_1 \approx 0.028$, $\tilde{A}_2 \approx 0.013$, and $\tilde{A}_3 \approx 1.45$. This fit is shown in Fig. 2(c) and it works quite well up to $U \lesssim t$. Similarly, in the $U/t \to \infty$ limit when $E_b = -U$, one can show that $M_b = 4/(a^2t_p)$, where $t_p = 2t^2/U$ is the effective hopping parameter for a strongly bound pair, as discussed above. This is consistent with our numerical finding $1/(a^2tM_b) \approx 0.0048$ when $U = 100t$. It is pleasing to note that this finding is also aligned with the effective-mass tensor of the highest Bloch band where $(m_1^{-1})_{ij} = a^2\ddot{\varepsilon}^{ij}_{1\mathbf{k}}|_{\mathbf{k}=\mathbf{0}} = (a^2\bar{t}/4)\delta_{ij}$.

## IV. MANY-BODY PROBLEM

It turns out the complex parameter $\beta_{S\ell\mathbf{q}}$ plays precisely the role of an order parameter for spin-singlet pairing on sublattice $S$ in the two-body problem [39]. In more general terms, the correspondence between the analogous parameters for the spin-singlet and -triplet two-body bound states and that of the spin-singlet and -triplet BCS order parameters can be found in Ref. [40] in the context of the extended-Hubbard model. Thus, given that the uniform-pairing condition is satisfied for the lowest-lying two-body bound states when $\mathbf{q} \to \mathbf{0}$, the analogous Cooper pairing and its many-body BCS mean-field extension (i.e., assuming stationary Cooper pairs with zero center-of-mass momentum) are also described by a uniform order parameter in a unit cell. We emphasize that the uniform-pairing condition is satisfied exactly in the two-body problem without any phase difference between the sublattices. This is in fact the underlying reason for the perfect agreement between Eqs. (4)–(7) and that of the numerics shown in Fig. 2(a).

### A. BCS-BEC crossover

For this reason, we take $\Delta_S \equiv \Delta_0$ as the uniform order parameter for superconductivity in all four sublattices and set it to a real positive number. Following the standard prescription, we obtain the mean-field self-consistency relations [24],

$$1 = \frac{U}{N}\sum_{n\mathbf{k}} \frac{\mathcal{X}_{n\mathbf{k}}}{2E_{n\mathbf{k}}}, \tag{10}$$

$$F = 1 - \frac{1}{N}\sum_{n\mathbf{k}} \frac{\mathcal{X}_{n\mathbf{k}}}{E_{n\mathbf{k}}}\xi_{n\mathbf{k}}, \tag{11}$$

where $\mathcal{X}_{n\mathbf{k}} = \tanh(\frac{E_{n\mathbf{k}}}{2T})$ is a thermal factor, with $k_B \to 1$ the Boltzmann constant and $T$ the temperature, $\xi_{n\mathbf{k}} = \varepsilon_{n\mathbf{k}} - \mu$ is the shifted dispersion with $\mu$ the chemical potential, $E_{n\mathbf{k}} = \sqrt{\xi_{n\mathbf{k}}^2 + \Delta_0^2}$ is the intraband quasiparticle spectrum, and the particle filling $0 \leqslant F = \mathcal{N}/N \leqslant 2$ corresponds to the total number of particles per site. Note that there is no interband pairing since the underlying time-reversal symmetry guarantees the presence of a $\downarrow$ particle in Bloch state $|n_{-\mathbf{k}}\rangle$ for every $\uparrow$ particle in $|n_{\mathbf{k}}\rangle$, as the energetically most favorable BCS scenario for the stationary pairs. Self-consistent solutions of Eqs. (10) and (11) for $\Delta_0$ and $\mu$ are the starting point of the BCS-BEC crossover theories, and they are known to produce qualitatively correct results at sufficiently low $T$ including the $U/t \to \infty$ limit. In addition, the mean-field expression for the filling of condensed particles [24,41],

$$F_c = \frac{\Delta_0^2}{N}\sum_{n\mathbf{k}} \frac{\mathcal{X}_{n\mathbf{k}}^2}{2E_{n\mathbf{k}}^2}, \tag{12}$$

plays an important role in our discussion below and it also produces qualitatively correct results at all $U \neq 0$ as long as $T$ is sufficiently low.

### B. Superfluid weight

When the uniform-pairing condition is met together with the time-reversal symmetry, the superfluid phase-stiffness tensor, often called the superfluid weight, can be written as $\mathcal{D}_{ij} = \mathcal{D}_{ij}^{\text{intra}} + \mathcal{D}_{ij}^{\text{inter}}$, depending on whether the intraband or interband processes are involved. Using a linear-response theory and Kubo formalism or by simply imposing a phase twist in the order parameter [23,24,42], it can be shown that

$$\mathcal{D}_{ij}^{\text{intra}} = \frac{\Delta_0^2}{\mathcal{V}}\sum_{n\mathbf{k}}\left(\frac{\mathcal{X}_{n\mathbf{k}}}{E_{n\mathbf{k}}^3} - \frac{\mathcal{Y}_{n\mathbf{k}}}{2TE_{n\mathbf{k}}^2}\right)\dot{\xi}^i_{n\mathbf{k}}\dot{\xi}^j_{n\mathbf{k}}, \tag{13}$$

$$\mathcal{D}_{ij}^{\text{inter}} = \frac{\Delta_0^2}{\mathcal{V}}\sum_{n,m\neq n,\mathbf{k}}\left(\frac{\mathcal{X}_{n\mathbf{k}}}{E_{n\mathbf{k}}} - \frac{\mathcal{X}_{n\mathbf{k}} - \mathcal{X}_{m\mathbf{k}}}{E_{n\mathbf{k}} - E_{m\mathbf{k}}}\right) \times \frac{(\xi_{n\mathbf{k}} - \xi_{m\mathbf{k}})^2}{E_{m\mathbf{k}}(E_{n\mathbf{k}} + E_{m\mathbf{k}})}g_{ij}^{nm\mathbf{k}}, \tag{14}$$

where $\mathcal{Y}_{n\mathbf{k}} = \text{sech}^2(\frac{E_{n\mathbf{k}}}{2T})$ is another thermal factor. Thus, similar to the inverse effective-mass tensor of the lowest-lying two-body branch, the intraband contribution depends only on the derivatives of the Bloch spectrum, but the interband contribution also depends on the band-resolved quantum-metric tensor. For this reason, the former (latter) is also referred to as the conventional (geometric) contribution [8,23]. This is partly because Eq. (13) can be written in a more familiar form, i.e., through some integration by parts and algebra, $\mathcal{D}_{ij}^{\text{intra}} = \frac{\Delta_0^2}{\mathcal{V}}\sum_{n\mathbf{k}}[\ddot{\xi}^{ij}_{n\mathbf{k}}(1 - \mathcal{X}_{n\mathbf{k}}\xi_{n\mathbf{k}}/E_{n\mathbf{k}}) - \mathcal{Y}_{n\mathbf{k}}\dot{\xi}^i_{n\mathbf{k}}\dot{\xi}^j_{n\mathbf{k}}/(2T)]$, which is simply a sum over the the well-known single-band expression [19]. Next we show that the geometric origin of the superfluid weight, i.e., Eq. (14), can be traced all the way back to the effective mass of the superfluid carriers.

#### *1. $T \to 0$ limit*

Let us first analyze Eqs. (13) and (14) at $T = 0$. Assuming $\Delta_0 \neq 0$, we may set $\mathcal{X}_{n\mathbf{k}} = 1$ and $\mathcal{Y}_{n\mathbf{k}} = 0$, leading to

$$\mathcal{D}_{ij} = \frac{2\Delta_0^2}{\mathcal{V}}\sum_{nm\mathbf{k}} \frac{\text{Re}\big[\langle n_{\mathbf{k}}|\dot{\mathbf{h}}^i_{\mathbf{k}}|m_{\mathbf{k}}\rangle\langle m_{\mathbf{k}}|\dot{\mathbf{h}}^j_{\mathbf{k}}|n_{\mathbf{k}}\rangle\big]}{E_{m\mathbf{k}}(E_{n\mathbf{k}} + E_{m\mathbf{k}})} \tag{15}$$

for the total superfluid weight, where $\dot{\mathbf{h}}^i_{\mathbf{k}} = \partial\mathbf{h}_{\mathbf{k}}/\partial k_i$ is the derivative of the Hamiltonian matrix. Here we concentrate on two physically transparent limits. The first one is the $U/t \to \infty$ limit, where $\Delta_0 = \frac{U}{2}\sqrt{F(2-F)}$

and $\mu = -\frac{U}{2}(1-F)$ such that $\sqrt{\mu^2+\Delta_0^2} = U/2$. For this reason, we may set $E_{n\mathbf{k}} \to \sqrt{\mu^2+\Delta_0^2}$ in Eq. (15), and calculate $\sum_{nm\mathbf{k}}[\langle n_\mathbf{k}|\dot{\mathbf{h}}^i_\mathbf{k}|m_\mathbf{k}\rangle\langle m_\mathbf{k}|\dot{\mathbf{h}}^j_\mathbf{k}|n_\mathbf{k}\rangle] = \sum_\mathbf{k}\mathrm{Tr}[\dot{\mathbf{h}}^i_\mathbf{k}\dot{\mathbf{h}}^j_\mathbf{k}] = N_c a^2 t^2 \delta_{ij}$, leading eventually to $\mathcal{D}_{ij} = \mathcal{D}_0\delta_{ij}$ where $\mathcal{D}_0 = 8F(2-F)t^2/(aU)$. This result can be understood as follows. In the case of a continuum model with a single parabolic dispersion $\varepsilon_\mathbf{k} = k^2/(2m_0)$ and an attractive $s$-wave contact interaction between particles, it can be shown that $\mathcal{D}_0 = \rho_0/m_0$, where $\rho_0$ is the superfluid density. When these particles form strongly bound, weakly interacting pairs in the BEC limit, we may set $\rho_p = \rho_0/2$ as the superfluid density of pairs and $M_p = 2m_0$ as their mass, leading to $\mathcal{D}_0 = 4\rho_p/M_p$ in terms of the pair properties [24,25]. Furthermore, given that all of the particles participate in the superfluid flow at $T=0$ for any interaction strength in a continuum model [43], i.e., $\rho_0 = \mathcal{N}/\mathcal{V} = 16F/a^3$ where $F$ is the filling of superfluid particles in the corresponding lattice model, we expect $\rho_p = 16F_p/a^3$ where $F_p$ is the filling of superfluid pairs. Moreover, substituting $F_c/2 = F(2-F)/4$ as $F_p$ in the $U/t\to\infty$ limit, we identify $M_p = 2U/(a^2t^2)$ as the effective mass of the superfluid pairs in a pyrochlore lattice. It is pleasing to see that this analysis is in full agreement with $M_b = 2U/(a^2t^2)$ of the effective band mass of the lowest-lying two-body branch presented in Sec. III.

The second limit is the extremely low particle-filling $F\to 0$ case and its extremely high particle-filling $F\to 2$ counterpart (which is equivalently to the extremely low hole filling), where $\mu \leqslant -2t$ and $\xi_{n\mathbf{k}} \geqslant 0$ in the former and $\mu \geqslant 6t$ and $\xi_{n\mathbf{k}} \leqslant 0$ in the latter, with $|\xi_{n\mathbf{k}}| \gg \Delta_0$ for any $U\neq 0$. For this reason, we may set $E_{n\mathbf{k}} \to |\xi_{n\mathbf{k}}|$ and obtain

$$\mathcal{D}^{\mathrm{intra}}_{ij} = \frac{\Delta_0^2}{\mathcal{V}}\sum_{n\mathbf{k}}\frac{\dot{\xi}^i_{n\mathbf{k}}\dot{\xi}^j_{n\mathbf{k}}}{|\xi_{n\mathbf{k}}|^3} = \frac{\Delta_0^2}{2\mathcal{V}}\sum_{n\mathbf{k}}\frac{|\ddot{\xi}^{ij}_{n\mathbf{k}}|}{\xi^2_{n\mathbf{k}}}, \tag{16}$$

$$\mathcal{D}^{\mathrm{inter}}_{ij} = \frac{2\Delta_0^2}{\mathcal{V}}\sum_{n\mathbf{k}}\frac{g^{n\mathbf{k}}_{ij}}{|\xi_{n\mathbf{k}}|} - \frac{4\Delta_0^2}{\mathcal{V}}\sum_{n,m\neq n,\mathbf{k}}\frac{g^{nm\mathbf{k}}_{ij}}{|\xi_{n\mathbf{k}}|+|\xi_{m\mathbf{k}}|}, \tag{17}$$

where we used integration by parts in Eq. (16), and $g^{nm\mathbf{k}}_{ij} = g^{mn\mathbf{k}}_{ji}$ and $g^{n\mathbf{k}}_{ij} = g^{n\mathbf{k}}_{ji}$ in the evaluation of Eq. (17). In addition, using the density of superfluid pairs $\rho_p = NF_p/\mathcal{V}$ along with $F_p = F_c/2 = \frac{\Delta_0^2}{4N}\sum_{n\mathbf{k}}\frac{1}{\xi^2_{n\mathbf{k}}}$, we eventually find

$$\mathcal{D}_{ij} = 4\rho_p\big(M_b^{-1}\big)_{ij} \tag{18}$$

for the $F\to 0$ limit, where $(M_b^{-1})_{ij} = (M^{-1}_{\mathrm{intra}})_{ij} + (M^{-1}_{\mathrm{inter}})_{ij}$ is precisely determined as the inverse effective-mass tensor of the lowest-lying two-particle bound states. This can be seen by setting $\mu = E_b/2$ and $\ddot{\xi}^{ij}_{n\mathbf{k}} = \ddot{\varepsilon}^{ij}_{n\mathbf{k}}$ in Eqs. (6) and (7). Note that the $F\to 2$ limit is similar, but with the appearance of the inverse effective-mass tensor of the highest-lying two-hole branch.

#### 2. $T\to T_c$ limit

Let us also analyze Eqs. (13) and (14) in the vicinity of the critical superconducting transition temperature $T_c$. Since $\Delta_0/t\to 0^+$ in the $T\to T_c$ limit from below, we may set $E_{n\mathbf{k}}\to|\xi_{n\mathbf{k}}|$ and obtain

$$\mathcal{D}^{\mathrm{intra}}_{ij} = \frac{\Delta_0^2}{\mathcal{V}}\sum_{n\mathbf{k}}\left[\left(\frac{X_{n\mathbf{k}}}{2\xi^2_{n\mathbf{k}}} - \frac{Y_{n\mathbf{k}}}{4T\xi_{n\mathbf{k}}}\right)\ddot{\xi}^{ij}_{n\mathbf{k}} + \frac{X_{n\mathbf{k}}Y_{n\mathbf{k}}}{4T^2\xi_{n\mathbf{k}}}\dot{\xi}^i_{n\mathbf{k}}\dot{\xi}^j_{n\mathbf{k}}\right], \tag{19}$$

$$\mathcal{D}^{\mathrm{inter}}_{ij} = \frac{2\Delta_0^2}{\mathcal{V}}\sum_{n\mathbf{k}}\frac{X_{n\mathbf{k}}}{\xi_{n\mathbf{k}}}g^{n\mathbf{k}}_{ij} - \frac{2\Delta_0^2}{\mathcal{V}}\sum_{n,m\neq n,\mathbf{k}}\frac{X_{n\mathbf{k}}+X_{m\mathbf{k}}}{\xi_{n\mathbf{k}}+\xi_{m\mathbf{k}}}g^{nm\mathbf{k}}_{ij}, \tag{20}$$

where $X_{n\mathbf{k}} = \tanh\left(\frac{\xi_{n\mathbf{k}}}{2T}\right)$ and $Y_{n\mathbf{k}} = \mathrm{sech}^2\left(\frac{\xi_{n\mathbf{k}}}{2T}\right)$. Here we used integration by parts, $\sum_\mathbf{k} X_{n\mathbf{k}}\dot{\xi}^i_{n\mathbf{k}}\dot{\xi}^j_{n\mathbf{k}}/\xi^3_{n\mathbf{k}} = \sum_\mathbf{k} Y_{n\mathbf{k}}\dot{\xi}^i_{n\mathbf{k}}\dot{\xi}^j_{n\mathbf{k}}/(4T\xi^2_{n\mathbf{k}}) + \sum_\mathbf{k} X_{n\mathbf{k}}\ddot{\xi}^{ij}_{n\mathbf{k}}/(2\xi^2_{n\mathbf{k}})$, that is followed by another integration by parts, $\sum_\mathbf{k} Y_{n\mathbf{k}}\dot{\xi}^i_{n\mathbf{k}}\dot{\xi}^j_{n\mathbf{k}}/\xi^2_{n\mathbf{k}} = -\sum_\mathbf{k} X_{n\mathbf{k}}Y_{n\mathbf{k}}\dot{\xi}^i_{n\mathbf{k}}\dot{\xi}^j_{n\mathbf{k}}/(T\xi_{n\mathbf{k}}) + \sum_\mathbf{k} Y_{n\mathbf{k}}\ddot{\xi}^{ij}_{n\mathbf{k}}/\xi_{n\mathbf{k}}$ in Eq. (19), and $g^{nm\mathbf{k}}_{ij} = g^{mn\mathbf{k}}_{ji}$ and $g^{n\mathbf{k}}_{ij} = g^{n\mathbf{k}}_{ji}$ in the evaluation of Eq. (20). Note that Eqs. (19) and (20) reproduce, respectively, Eqs. (16) and (17) in the limit when $|\xi_{n\mathbf{k}}|\gg T_c$, e.g., in the $U/t\to\infty$ where $T_c/t\propto t/U\to 0$. It is also pleasing to see that

$$\mathcal{D}_{ij} = \frac{4N_c\Delta_0^2}{\mathcal{V}}\mathcal{C}_{ij}, \tag{21}$$

where $\mathcal{C}_{ij} = \mathcal{C}^{\mathrm{intra}}_{ij} + \mathcal{C}^{\mathrm{inter}}_{ij}$ is precisely the kinetic coefficient that appears in the Ginzburg-Landau theory near $T_c$ [44], determining not only the superfluid density and effective mass of the superfluid carriers, but also the coherence length, magnetic penetration depth, upper critical magnetic field, etc. Notably, certain among these quantities have already been measured to characterize geometric effects in twisted bilayer graphene [45].

We note in passing that it is desirable to have an analytic expression for $\mathcal{C}_{ij}$ in the $U/t\to 0$ limit. However, due to the complex nature of the pyrochlore lattice, which features four Bloch bands with nonisolated flat bands touching dispersive bands, and dispersive bands exhibiting highly anisotropic momentum dependence within a nontrivial BZ that is in the shape of a truncated octahedron, evaluating $\mathcal{C}_{ij}$ poses a significant challenge. Moreover, numerically computing $\mathcal{C}_{ij}$ necessitates a self-consistent determination of $T_c$ and $\mu$, which, in principle, can be achieved by extending the Nozieres-Schmitt-Rink approach to the multiband case [46,47]. Unfortunately, this extension is also highly nontrivial and its numerical implementation may encounter challenging convergence issues. Therefore, we primarily focus on the $T=0$ case in this paper, which is comparatively more manageable.

### C. Low-lying Goldstone modes at $T=0$

Similar to the superfluid weight, next we show that the low-energy collective modes also have a quantum-geometric origin [48]. As discussed in Appendix A, the dispersion $\omega_\mathbf{q}$ for the collective Goldstone modes is determined by the poles of the fluctuation propagator, $\boldsymbol{\mathcal{M}}_q^{-1}$, i.e., by setting $\det\boldsymbol{\mathcal{M}}_q = 0$, after an analytic continuation $\mathrm{i}\nu_n\to\omega+\mathrm{i}0^+$

to the real axis. At $T=0$, the matrix elements of $\boldsymbol{\mathcal{M}}_q$ reduce to

$$\mathcal{M}_{11}^{q,E}=\frac{4}{U}+\frac{1}{N_c}\sum_{nm\mathbf{k}}\frac{(\xi\xi'+EE')(E+E')|\langle n_{\mathbf{k}}|m_{\mathbf{k}-\mathbf{q}}\rangle|^2}{2EE'[\omega^2-(E+E')^2]}, \tag{22}$$

$$\mathcal{M}_{11}^{q,O}=\frac{1}{N_c}\sum_{nm\mathbf{k}}\frac{(\xi E'+E\xi')\omega|\langle n_{\mathbf{k}}|m_{\mathbf{k}-\mathbf{q}}\rangle|^2}{2EE'[\omega^2-(E+E')^2]}, \tag{23}$$

$$\mathcal{M}_{12}^{q}=-\frac{1}{N_c}\sum_{nm\mathbf{k}}\frac{\Delta_0^2(E+E')|\langle n_{\mathbf{k}}|m_{\mathbf{k}-\mathbf{q}}\rangle|^2}{2EE'[\omega^2-(E+E')^2]}, \tag{24}$$

where we denote $\xi_{n\mathbf{k}}$ by $\xi$, $\xi_{m,\mathbf{k}-\mathbf{q}}$ by $\xi'$, $E_{n\mathbf{k}}$ by $E$, and $E_{m,\mathbf{k}-\mathbf{q}}$ by $E'$. To determine the lowest-energy Goldstone modes, it is sufficient to retain terms up to quadratic order in their small-$\mathbf{q}$ and $\omega$ expansions, leading to $\mathcal{M}_{11}^{q,E}+\mathcal{M}_{12}^{q}=A+\sum_{ij}C_{ij}q_iq_j-D\omega^2$, $\mathcal{M}_{11}^{q,E}-\mathcal{M}_{12}^{q}=\sum_{ij}Q_{ij}q_iq_j-R\omega^2$ and $\mathcal{M}_{11}^{q,O}=-B\omega$. In the expansion of $\mathcal{M}_{11}^{q,E}-\mathcal{M}_{12}^{q}$, the zeroth-order term vanishes due to the saddle-point condition given in Eq. (10). The nonkinetic expansion coefficients $A=\frac{1}{N_c}\sum_{n\mathbf{k}}\Delta_0^2/(2E_{n\mathbf{k}}^3)$, $B=\frac{1}{N_c}\sum_{n\mathbf{k}}\xi_{n\mathbf{k}}/(4E_{n\mathbf{k}}^3)$, $D=\frac{1}{N_c}\sum_{n\mathbf{k}}\xi_{n\mathbf{k}}^2/(8E_{n\mathbf{k}}^5)$, and $R=\frac{1}{N_c}\sum_{n\mathbf{k}}1/(8E_{n\mathbf{k}}^3)$ are simply given by a sum of their single-band counterparts [49]. When $B^2\ll AR$, it is clearly seen that the phase and amplitude modes are decoupled, and this is known to be the case only in the strict BCS limit [49].

Similar to the superfluid weight, the kinetic coefficients can be written as $Q_{ij}=Q_{ij}^{\text{intra}}+Q_{ij}^{\text{inter}}$ and $C_{ij}=C_{ij}^{\text{intra}}+C_{ij}^{\text{inter}}$, depending on whether the intraband or interband processes are involved, leading to

$$Q_{ij}^{\text{intra}}=\frac{1}{N_c}\sum_{n\mathbf{k}}\frac{1}{8E_{n\mathbf{k}}^3}\dot{\xi}_{n\mathbf{k}}^i\dot{\xi}_{n\mathbf{k}}^j, \tag{25}$$

$$Q_{ij}^{\text{inter}}=\frac{1}{N_c}\sum_{n,m\neq n,\mathbf{k}}\frac{(\xi_{n\mathbf{k}}-\xi_{m\mathbf{k}})^2}{8E_{n\mathbf{k}}E_{m\mathbf{k}}(E_{n\mathbf{k}}+E_{m\mathbf{k}})}g_{ij}^{nm\mathbf{k}}, \tag{26}$$

$$C_{ij}^{\text{intra}}=\frac{1}{N_c}\sum_{n\mathbf{k}}\frac{1}{8E_{n\mathbf{k}}^3}\left(1-\frac{5\Delta_0^2\xi_{n\mathbf{k}}^2}{E_{n\mathbf{k}}^4}\right)\dot{\xi}_{n\mathbf{k}}^i\dot{\xi}_{n\mathbf{k}}^j, \tag{27}$$

$$C_{ij}^{\text{inter}}=-\frac{1}{N_c}\sum_{n\mathbf{k}}\frac{\Delta_0^2}{4E_{n\mathbf{k}}}g_{ij}^{n\mathbf{k}}+\frac{1}{N_c}\sum_{n,m\neq n,\mathbf{k}}\frac{(\xi_{n\mathbf{k}}-\xi_{m\mathbf{k}})^2+4\Delta_0^2}{8E_{n\mathbf{k}}E_{m\mathbf{k}}(E_{n\mathbf{k}}+E_{m\mathbf{k}})}g_{ij}^{nm\mathbf{k}}. \tag{28}$$

Here the geometric contributions follow from the small-$\mathbf{q}$ expansion given in Eq. (9) [50]. Furthermore, the intraband coefficients can also be put in the more familiar forms, i.e., again through some integration by parts and algebra, $Q_{ij}^{\text{intra}}=\frac{1}{N_c}\sum_{n\mathbf{k}}[\xi_{n\mathbf{k}}\ddot{\xi}_{n\mathbf{k}}^{ij}-\dot{\xi}_{n\mathbf{k}}^i\dot{\xi}_{n\mathbf{k}}^j(1-3\Delta_0^2/E_{n\mathbf{k}}^2)]/(8E_{n\mathbf{k}}^3)$ and $C_{ij}^{\text{intra}}=\frac{1}{N_c}\sum_{n\mathbf{k}}[\xi_{n\mathbf{k}}(1-3\Delta_0^2/E_{n\mathbf{k}}^2)\ddot{\xi}_{n\mathbf{k}}^{ij}-\dot{\xi}_{n\mathbf{k}}^i\dot{\xi}_{n\mathbf{k}}^j(1-10\Delta_0^2\xi_{n\mathbf{k}}^2/E_{n\mathbf{k}}^4)]/(8E_{n\mathbf{k}}^3)$, which are simply sums of their well-known single-band expressions [48,49]. By setting $\det\boldsymbol{\mathcal{M}}_q=0$, we obtain

$$\omega_{\mathbf{q}}^2=\sum_{ij}\frac{Q_{ij}}{R+B^2/A}q_iq_j, \tag{29}$$

which is the dispersion for the low-momentum and low-frequency Goldstone modes. Thus, we are pleased to verify that the low-energy collective excitations have a linear dispersion whose finite velocity is characterized by the superfluid weight, i.e.,

$$\mathcal{D}_{ij}=\frac{8N_c\Delta_0^2}{\mathcal{V}}Q_{ij}, \tag{30}$$

at zero temperature.

We note in passing that the stability of the Goldstone modes is ensured by the stability of the superconducting state, as follows. In the long-wavelength limit, the effective action associated with the phase fluctuations of the order parameter can be expressed as $\mathcal{S}_\theta=\frac{1}{8}\int_0^{1/T}d\tau\int d^3\mathbf{r}\sum_{ij}\mathcal{D}_{ij}\dot{\theta}^i\dot{\theta}^j$, where $\mathbf{r}=(x,y,z)$ denotes the position in real space and $\dot{\theta}^i=\partial\theta(\mathbf{r},\tau)/\partial r_i$ controls the spatial variations of the phase [23,51]. By definition, this implies that $\mathcal{D}_{ij}$ determines the response of the superconducting system to a phase twist of the order parameter, i.e., the response of the thermodynamic potential to an infinitesimal superfluid flow [52]. Therefore, the stability of a spatially uniform superfluid necessitates a positive definite $\mathcal{D}_{ij}$, as a negative eigenvalue indicates that the superconducting state is unstable towards a spontaneously generated phase gradient, i.e., towards a spatially nonuniform superfluid. Moreover, a positive definite $\mathcal{D}_{ij}$ ensures a positive speed for the Goldstone modes through Eq. (30), which is in accordance with the Landau's criterion for superfluidity.

## V. NUMERICAL RESULTS

In this section, we exclusively set $T=0$ and determine $\Delta_0$ and $\mu$ self-consistently from Eqs. (10) and (11), and then plug them into Eqs. (13) and (14) as a function of $U$. Typical solutions are shown in Fig. 3. When particle filling lies within the flat bands, i.e., when $\mu=-2t$ or, equivalently, $0\leqslant F\leqslant 1$ at $U=0$, it can be shown that [53] $\Delta_0=\frac{U}{2}\sqrt{F(1-F)}$, $\mu=-2t-\frac{U}{2}(\frac{1}{2}-F)$, and $F_c=F(1-F)$ in the $U/t\to 0$ limit. Note that these expressions are quite similar to those of the $U/t\to\infty$ limit's results because, given that $U/W\gg 1$ with $W\to 0$ being the bandwidth of a flat band, even an arbitrarily small but finite $U\neq 0$ corresponds effectively to a strong-coupling limit. Accordingly, when $\mu=-2t$ coincides perfectly with a flat band at $U=0$ (or, equivalently, corresponds to $F=0.5$, i.e., to half-filled flat bands), $\Delta_0$ grows linearly with $U$, as shown in Fig. 3(a). In this case, our numerical fit $a\mathcal{D}_0/t=\tilde{B}_1(U/t)-\tilde{B}_2(U/t)^{\tilde{B}_3}$ for $U/t\leqslant 0.1$ shows that $\tilde{B}_1\approx 0.225$, $\tilde{B}_2\approx 0.0544$, and $\tilde{B}_3\approx 1.44$, and this fit works very well up to $U\lesssim 2t$. This finding is in sharp contrast with the recent results on two-dimensional lattices, where a band touching with a flat band causes logarithmic corrections to the linear-in-$U$ term that is expected for an energetically isolated flat band in any dimension [25,26]. It is pleasing to see that this fit is quite similar in structure to that of $1/M_b$ of the two-body problem discussed in Sec. III, where $\tilde{B}_3\approx\tilde{A}_3$. The ratios $\tilde{B}_1/\tilde{B}_2$ and $\tilde{A}_1/\tilde{A}_2$ are not expected to be similar unless $F\to 0$.

It can also be shown that while the BCS order parameter $\Delta_0$ grows exponentially $e^{-1/[U\text{DOS}(\mu)]}$ slow when $-2t<\mu<2t$ and $2t<\mu<6t$ lies within any of the dispersive

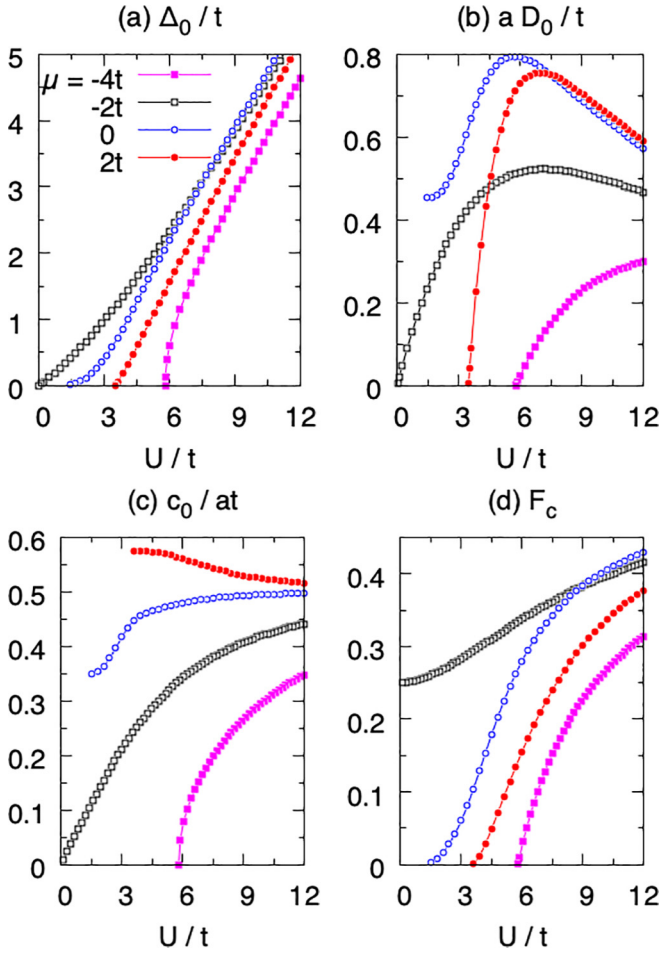


FIG. 3. (a) Order parameter $\Delta_0$, (b) isotropic superfluid weight $\mathcal{D}_0$, (c) isotropic sound speed $c_0$, and (d) filling of condensed particles $F_c$ as a function of $U$ at $T = 0$. Note that the disappearance of superconductivity is signalled by both $\Delta_0 \to 0$ and $\mathcal{D}_0 \to 0$ below the critical semimetal point $U_c \approx 3.48t$ when $\mu = 2t$.

Bloch bands, it grows linearly $U - U_c$ fast from the critical semimetal point with $U_c \approx 3.48t$ when $\mu = 2t$ or, equivalently, $F = 3/2$, and with a square root $\sqrt{U - U_c}$ from the particle and hole vacuums when $\mu < -2t$ or $\mu > 6t$. For instance, $U_c \approx 5.79t$ when $\mu = -4t$. These are illustrated in Fig. 3(a). Thus, the semimetal state persists even at finite $U$ and superconductivity does not appear until a critical interaction threshold $U_c$. The corresponding $\mathcal{D}_0$ are shown in Fig. 3(b), where it saturates at sufficiently small $U/t$ when $\mu$ lies within any of the dispersive Bloch bands, and vanishes otherwise. The latter finding again signals the disappearance of superconductivity at a finite interval $U < U_c$.

In Fig. 4, we present maps of the superfluid weight $\mathcal{D}_0$ together with its $\mathcal{D}_0^{\text{intra}}$ and $\mathcal{D}_0^{\text{inter}}$ contributions as a function of $U$, $\mu$, and $F$. Due to technical difficulties, i.e., the accuracy of the numerical integration becomes unreliable when the exponential growth of $\Delta_0$ is not accurately captured by the nonlinear solver due to the convergence problems, we choose to present the data in the parameter regime where $\Delta_0 \geqslant 0.01t$. See Appendix B for more details. This is why Fig. 4 has white regions, e.g., in the lower panels, even though $F$ corresponds to a partially filled dispersive Bloch band in the $U/t \to 0$ limit where $\mathcal{D}_0$ is known to saturate. This drawback offers the advantage that the single-particle density of states DOS($\mu$), shown in Fig. 1(b), appears on the periphery of the white regions, including the flat bands at $\mu = -2t$, van Hove singularities at $\mu = \{0, 4t\}$ or, equivalently, at $F \approx \{1.19, 1.81\}$, and the critical semimetal point at $\mu = 2t$ or, equivalently, at $F = 3/2$. On the other hand, the peripheries of the particle and hole vacuums and the critical semimetal point are determined quite accurately in the upper panels since $\Delta_0$ vanishes very rapidly in their vicinity when $U \to U_c \neq 0$; e.g., see Fig. 3(a). This is also indicated by the nearly invisible white regions at the edges of the lower panels when $F \to 0$ or $F \to 2$.

In the small-$U/t$ regime, Fig. 4 clearly shows that while $\mathcal{D}_0^{\text{inter}}$ is the dominant contributor in the flat-band superconductivity, i.e., when $0 < F \leqslant 1$, $\mathcal{D}_0^{\text{intra}}$ dominates the usual superconductivity in general when $\mu$ lies within a dispersive band. However, both contributions are equally important in the large-$U/t$ regime, including the $U/t \to \infty$ limit (not shown). In fact, $\mathcal{D}_0^{\text{inter}} \sim 2.6\mathcal{D}_0^{\text{intra}}$ even at $U = 100t$. We checked that the total superfluid weight approaches $\mathcal{D}_0 = 8F(2-F)t^2/(aU)$ in the $U/t \to \infty$ limit, which is in perfect agreement with the analysis given in Sec. IV B 1. Since the filling of condensed particles $F_c$ plays a critical role in connecting $\mathcal{D}_0$ to the effective mass of the superfluid carriers, we also present its map in Fig. 5 as a function of $U$, $\mu$, and $F$. This figure verifies that $F_c = F(1-F)$ (derived above) saturates when $0 \leqslant F \leqslant 1$ in the $U/t \to 0$ limit as soon as $U \neq 0$, and that all of the particles are entirely condensed in a dilute flat-band superconductor, i.e., $F_c = F$ when $F \to 0$ in Fig. 5. Such a perfect condensation may occur only if the repulsive interaction between small Cooper pairs is negligible, which may be the underlying reason behind our finding in Sec. IV B 1 that $\mathcal{D}_{ij} = 4\rho_p(M_b^{-1})_{ij}$ is determined entirely by the effective mass of the lowest-lying two-body branch when $F \to 0$. This is in sharp contrast to the usual superconductors where $F_c$ corresponds to a negligible fraction of particles in the small-$U/t$ regime [41], which can also be seen in the $F > 1$ region in Fig. 5. We again checked that $F_c = F(2-F)$ in the $U/t \to \infty$ limit, which is in perfect agreement with the analysis given in Sec. IV B 1.

In Fig. 6, we present maps of the square $s_0 = Q_0/(R + B^2/A)$ of the isotropic sound speed $c_0$, together with its $s_0^{\text{intra}}$ and $s_0^{\text{inter}}$ contributions, as a function of $U$, $\mu$, and $F$. First of all, both $s_0^{\text{intra}}$ and $s_0$ saturate in the $U/t \to 0$ limit when $\mu$ lies within a dispersive band and $s_0^{\text{inter}}$ is small and negligible. These are expected from the well-known single-band results [54]. In addition, for a fixed $U/t$ in the small-$U/t$ regime, both $s_0^{\text{intra}}$ and $s_0$ exhibit faint but visible dips around the van Hove singularities, which are also consistent with the well-known single-band results [54]. On the other hand, when $\mu = -2t$ coincides perfectly with a flat band at $U = 0$, both $s_0^{\text{inter}}$ and $s_0$ grow from 0 with a power law (approximately quadratically) in $U$, but $s_0^{\text{intra}}$ remain small and negligible. Thus, $c_0$ vanishes linearly with $U$ in a flat-band superconductor in the $U/t \to 0$ limit, which is in sharp contrast to the usual dispersive case where it saturates. In order to characterize and understand this particular limit, we set $E_{n\mathbf{k}} \to \sqrt{(-2t-\mu)^2 + \Delta_0^2}$ for the flat $n = \{3, 4\}$ bands and take only their contributions into

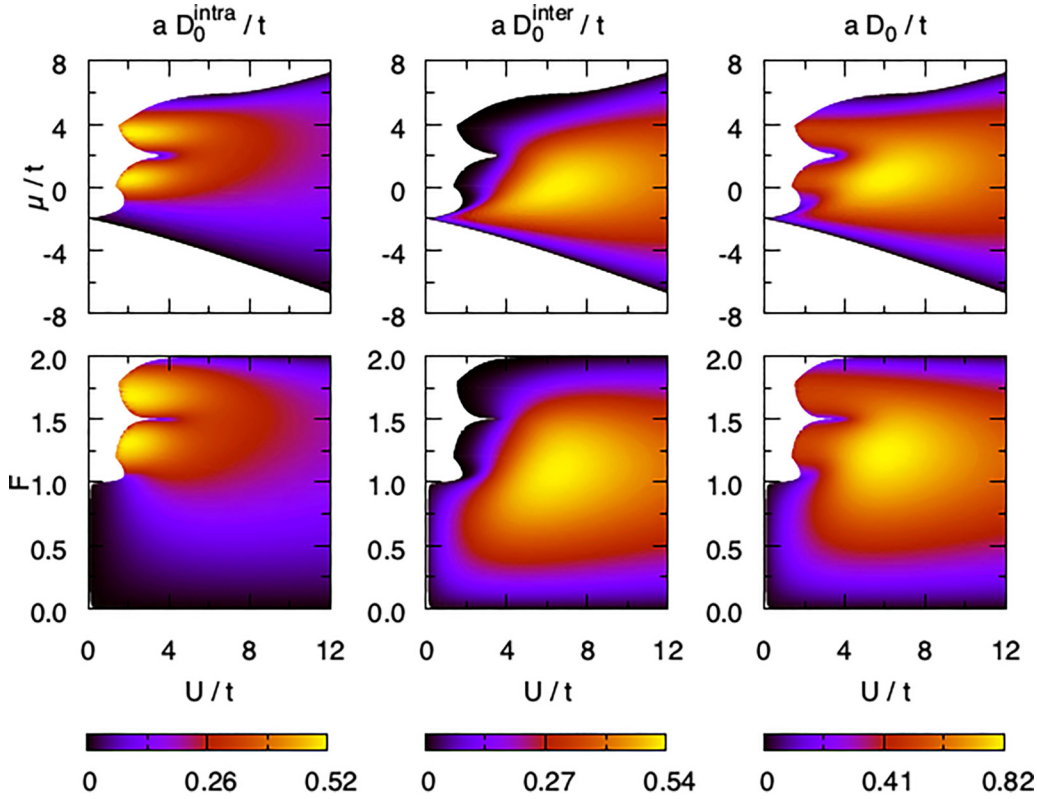


FIG. 4. Isotropic superfluid weight $\mathcal{D}_0$ together with its intraband and interband contributions as a function of $U$, $\mu$, and $F$ at $T = 0$. Since our numerical implementation becomes unreliable in the region where $\Delta_0$ is small, we choose to present those data that have $\Delta_0 \geqslant 0.01t$, which reveals the underlying DOS($\mu$) at the periphery of the white regions.

account, leading to $A = 16F(1-F)/U$, $B = 8(1-2F)/U^2$, and $R = 16/U^3$, where $0 \leqslant F \leqslant 1$. Furthermore, using the relation $\mathcal{D}_0 = 8U^2F(1-F)Q_0/a^3$, we find $s_0 = U\mathcal{D}_0a^3/32$, which is in perfect agreement with the numerics. In addition, at the semimetal critical point when $\mu = 2t$ and $U \to U_c$, both $s_0^{\text{intra}}$ and $s_0^{\text{inter}}$ exhibit comparable jumps from 0. Because of this, the resultant $s_0$ exhibits a much larger jump right at the tip of the critical region, since $s_0^{\text{inter}}$ is typically small and negligible in its vicinity. Lastly we consider the $U/t \to \infty$ limit and set $E_{n\mathbf{k}} \to \sqrt{\mu^2 + \Delta_0^2}$ for all bands, leading to $A = 4F(2-F)/U$, $B = 4(1-F)/U^2$, $R = 4/U^3$, and

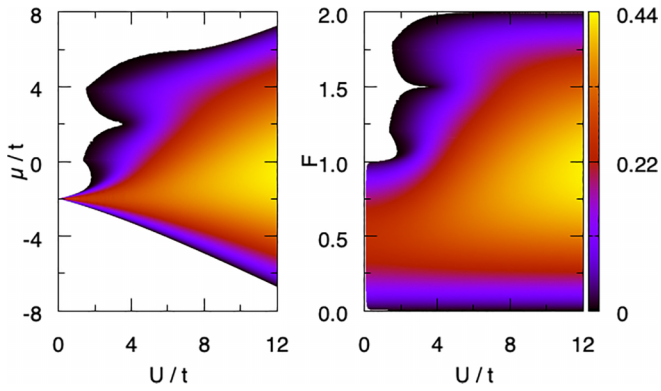


FIG. 5. The filling of condensed particles $F_c$ as a function of $U$, $\mu$, and $F$ at $T = 0$.

$Q_0 = a^2t^2/U^3$. The resultant $s_0 = a^2t^2F(2-F)/4$ depends only on $F$ as in the case of single-band case [54], and it is in perfect agreement with the numerics. It can be written in a form $s_0 = U\mathcal{D}_0a^3/32$ that is identical to the flat-band expression above. We also find it instructive to reinterpret the sound speed $c_0 = \sqrt{2UF_p/M_p}$ in terms of the filling $F_p$ and effective mass $M_p$ of the pairs. Then, by making a comparison with the Bogoliubov expression $c_B = \sqrt{U_BF_B/M_B}$ that is valid for a weakly interacting Bose gas on a tight-binding lattice [55], we identify $U_p = 2U$ as the parameter that characterizes the interaction between pairs in the $U/t \to \infty$ limit. Such a strong and repulsive on-site interaction between pairs of fermions can be attributed to the underlying Pauli exclusion principle [54]. On a similar footing, using the results of Sec. IV B 1, where $\mathcal{D}_0 = 4\rho_p/M_b$ for a dilute ($F \to 0$) flat-band superconductor when $U/t \to 0$, we also reach the conclusion that $U_p = 2U$. This suggests that the interaction between pairs tends to zero in a flat-band superconductor.

## VI. CONCLUSION

To summarize, we studied the impact of the quantum geometry of Bloch states, specifically through the band-resolved quantum-metric tensor, on Cooper pairing and flat-band superconductivity within a three-dimensional pyrochlore-Hubbard model. For this purpose, first we showed that the pairing order parameter is uniform in this four-band lattice through an exact calculation of the low-lying two-body spectrum. This simplification enabled us to reveal direct relations

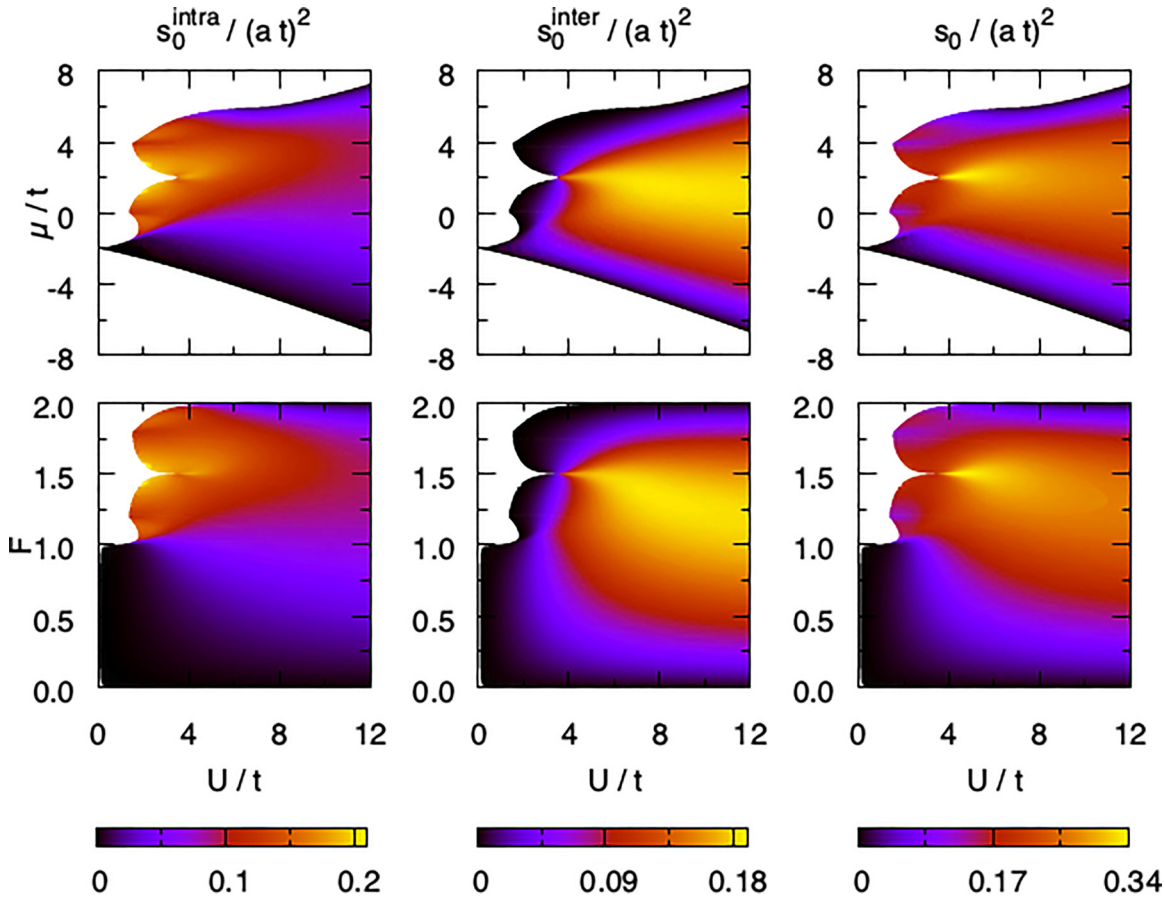


FIG. 6. Square $s_0 = Q_0/(R + B^2/A)$ of the isotropic sound speed together with its intraband and interband contributions as a function of $U$, $\mu$, and $F$ at $T = 0$.

between the superfluid weight of a multiband superconductor and (i) the effective mass of the lowest-lying two-body branch at $T = 0$ through $\mathcal{D}_{ij} = 4\rho_p(M_b^{-1})_{ij}$, (ii) the kinetic coefficient of the Ginzburg-Landau theory near $T_c$ through $\mathcal{D}_{ij} = \frac{4N_c\Delta_0^2}{\mathcal{V}}\mathcal{C}_{ij}$, and (iii) the velocity of the low-energy Goldstone modes at $T = 0$ through $\mathcal{D}_{ij} = \frac{8N_c\Delta_0^2}{\mathcal{V}}\mathcal{Q}_{ij}$. The underlying physics behind these relations is that a bound state with a finite center-of-mass momentum is a collective mode of the superfluid ground state. Then we presented a thorough numerical analysis of the superfluid weight and Goldstone modes together with their intraband (conventional) and interband (geometric) contributions at zero temperature. For instance, one of our important observations is that in sharp contrast to the recent results on two-dimensional lattices where a band touching with a flat band causes logarithmic corrections $\tilde{C}_1 U \ln(\tilde{C}_2/U)$ to the superfluid weight in the $U/t \to 0$ limit, the analogous correction is a power law in three dimensions which may be approximated by $\tilde{C}_1 U - \tilde{C}_2 U^{3/2}$. Another one is the relation $c_0 = \sqrt{U\mathcal{D}_0 a^3/32}$ between the sound speed and the superfluid weight in a flat-band superconductor when $U/t \to 0$, which further suggests that the interaction between pairs tends to zero.

Much like the well-explored two-dimensional toy models such as Mielke-checkerboard and kagome lattices, which display uniform pairing, we believe the pyrochlore lattice presents an excellent setting for conducting theoretical research on three-dimensional flat-band superconductivity. As an outlook, we are planning to develop a Ginzburg-Landau theory for the pyrochlore-Hubbard model and explore how quantum geometry affects not only the superfluid density and effective mass of the superfluid carriers, but also the coherence length, magnetic penetration depth, upper critical magnetic field, etc. in the BCS-BEC crossover [44].

## ACKNOWLEDGMENT

The author acknowledges funding from U.S. Air Force Office of Scientific Research (AFOSR) Grant No. FA8655-24-1-7391.

## APPENDIX A: GAUSSIAN FLUCTUATIONS

In order to go beyond the saddle-point (mean-field) approximation, we use imaginary-time functional path-integral formalism [48,49] and derive a quadratic effective action in the fluctuations of the order parameter for a multiband Hubbard model with on-site attraction. It turns out that this formalism is drastically simpler and transparent when the system manifests both time-reversal symmetry and the uniform-pairing condition as in the pyrochlore lattice of interest. In this case, the bosonic Hubbard-Stratonovich field (which plays the role of the order parameter) can be

split as

$$\Delta_{Sq} = \Delta_0 \delta_{q0} + \Lambda_q \tag{A1}$$

for all sublattice sites in a unit cell, where the complex field $\Lambda_q$ corresponds to the fluctuations around the stationary saddle-point parameter $\Delta_0$ (which is taken as real here and in the main text), and $q \equiv (\mathbf{q}, i\nu_\ell)$ is a collective index, with $\nu_\ell = 2\ell\pi T$ the bosonic Matsubara frequency. Given our interest in the low-energy in-phase (i.e., Goldstone) collective modes only, we also set $\Lambda_q$ to be uniform together with $\Delta_0$, making higher-energy out-of-phase (i.e., Leggett) collective modes inaccessible. In the case of a pyrochlore lattice, we expect three distinct Leggett branches to appear. In principle, they can be studied through an $S$-dependent $\Lambda_{Sq}$, but this is beyond the scope of this paper. See [48] for a similar analysis in two-band lattices, showing that the speed of the Leggett modes also has an interband contribution that is controlled by the quantum metric.

First we express the mean-field Hamiltonian $\mathcal{H}_{\rm mf}$ in the Bloch-band representation, whose Hamiltonian matrix can be expressed as [23]

$$\mathbf{H}^{\rm mf}_{\mathbf{k}} = \sum_n (\xi_{n\mathbf{k}}\tau_z + \Delta_0\tau_x) \otimes |n_{\mathbf{k}}\rangle\langle n_{\mathbf{k}}|, \tag{A2}$$

where $\tau_x$ and $\tau_z$ are Pauli matrices describing the particle-hole degrees of freedom. Then the saddle-point propagator can be written as $\mathcal{G}_0(k) = \sum_{sn} \frac{|\Psi^s_{n\mathbf{k}}\rangle\langle\Psi^s_{n\mathbf{k}}|}{i\omega_\ell - E^s_{n\mathbf{k}}}$, where $k \equiv (\mathbf{k}, i\omega_\ell)$ is a combined index with $\omega_\ell = (2\ell+1)\pi T$ the fermionic Matsubara frequency. Here, $\mathbf{H}^{\rm mf}_{\mathbf{k}}|\Psi^s_{n\mathbf{k}}\rangle = E^s_{n\mathbf{k}}|\Psi^s_{n\mathbf{k}}\rangle$ defines the quasiparticle-quasihole spectra $E^s_{n\mathbf{k}} = sE_{n\mathbf{k}}$ with $s = \pm$, where the associated eigenvectors are $|\Psi^+_{n\mathbf{k}}\rangle = \binom{u_{n\mathbf{k}}}{v_{n\mathbf{k}}} \otimes |n_{\mathbf{k}}\rangle$ for the quasiparticles and $|\Psi^-_{n\mathbf{k}}\rangle = \binom{-v_{n\mathbf{k}}}{u_{n\mathbf{k}}} \otimes |n_{\mathbf{k}}\rangle$ for the quasiholes. The coherence factors $u_{n\mathbf{k}} = \sqrt{\frac{1}{2} + \frac{\xi_{n\mathbf{k}}}{E_{n\mathbf{k}}}}$ and $v_{n\mathbf{k}} = \sqrt{\frac{1}{2} - \frac{\xi_{n\mathbf{k}}}{E_{n\mathbf{k}}}}$ coincide with the usual intraband expressions due to the absence of interband pairing.

Following the standard procedure, the quadratic effective action can be written as $\mathcal{S}_2 = \frac{N_S}{TU}\sum_q |\Lambda_q|^2 + \frac{1}{2N_c}\mathrm{Tr}\sum_{kq} \mathcal{G}_0(k)\mathbf{\Sigma}(q)\mathcal{G}_0(k-q)\mathbf{\Sigma}(-q)$, where Tr denotes a trace over the band and particle-hole sectors, and $\mathbf{\Sigma}(q) = (\Lambda_q\tau_+ + \Lambda^*_{-q}\tau_-) \otimes \mathcal{I}_{N_S}$ is controlled purely by the fluctuation fields. Here, $N_S$ is the number of sublattices in a unit cell (which is four for the pyrochlore lattice), $\tau_\pm = (\tau_x \pm i\tau_y)/2$, and $\mathcal{I}_{N_S}$ is an $N_S \times N_S$ unit matrix in the band space. Upon evaluation of the trace and sum over the fermionic frequencies, we eventually obtain

$$\mathcal{S}_2 = \frac{1}{2T}\sum_q (\Lambda^*_q\ \Lambda_{-q}) \begin{pmatrix} \mathcal{M}^{11}_q & \mathcal{M}^{12}_q \\ \mathcal{M}^{21}_q & \mathcal{M}^{22}_q \end{pmatrix} \begin{pmatrix} \Lambda_q \\ \Lambda^*_{-q} \end{pmatrix}, \tag{A3}$$

where the fluctuation matrix $\boldsymbol{\mathcal{M}}_q$ plays the role of inverse propagator of amplitude and phase fluctuations. In order to express its matrix elements in a compact form, we denote $\xi_{n\mathbf{k}}$ by $\xi$, $\xi_{m,\mathbf{k}-\mathbf{q}}$ by $\xi'$, $E_{n\mathbf{k}}$ by $E$, $E_{m,\mathbf{k}-\mathbf{q}}$ by $E'$, and denote their functions as $u^2 = (1+\xi/E)/2$, $u'^2 = (1+\xi'/E')/2$, $v^2 = (1-\xi/E)/2$, $v'^2 = (1-\xi'/E')/2$, $f = 1/(e^{E/T}+1)$, and $f' = 1/(e^{E'/T}+1)$, leading to

$$\mathcal{M}^q_{11} = \mathcal{M}^{-q}_{22} = \frac{N_S}{U} + \frac{1}{N_c}\sum_{nm\mathbf{k}} |\langle n_{\mathbf{k}}|m_{\mathbf{k}-\mathbf{q}}\rangle|^2 \times \left[(1-f-f')\left(\frac{u^2u'^2}{i\nu_\ell - E - E'} - \frac{v^2v'^2}{i\nu_\ell + E + E'}\right) + (f-f')\left(\frac{v^2u'^2}{i\nu_\ell + E - E'} - \frac{u^2v'^2}{i\nu_\ell - E + E'}\right)\right], \tag{A4}$$

$$\mathcal{M}^q_{12} = \mathcal{M}^q_{21} = \frac{1}{N_c}\sum_{nm\mathbf{k}} |\langle n_{\mathbf{k}}|m_{\mathbf{k}-\mathbf{q}}\rangle|^2 \times \left[(1-f-f')\left(\frac{uvu'v'}{i\nu_\ell + E + E'} - \frac{uvu'v'}{i\nu_\ell - E - E'}\right) + (f-f')\left(\frac{uvu'v'}{i\nu_\ell + E - E'} - \frac{uvu'v'}{i\nu_\ell - E + E'}\right)\right]. \tag{A5}$$

Note that while $\mathcal{M}^q_{12}$ is even both under $\mathbf{q} \to -\mathbf{q}$ and $i\nu_\ell \to -i\nu_\ell$, $\mathcal{M}^q_{11}$ is even only under $\mathbf{q} \to -\mathbf{q}$. In the presence of a single band, these expressions recover the usual results [48,49].

Next we introduce a unitary transformation $\Lambda_q = (\lambda_q + i\theta_q)/\sqrt{2}$, and associate $\lambda_q$ and $\theta_q$ with the amplitude and phase degrees of freedom, respectively. Assuming these are real functions in real space and time, we set $\lambda_{-q} = \lambda^*_q$ and $\theta_{-q} = \theta^*_q$, and express the effective action in the form

$$\sum_q (\lambda^*_q\ \theta^*_q) \begin{pmatrix} \mathcal{M}^{q,E}_{11} + \mathcal{M}^q_{12} & i\mathcal{M}^{q,O}_{11} \\ -i\mathcal{M}^{q,O}_{11} & \mathcal{M}^{q,E}_{11} - \mathcal{M}^q_{12} \end{pmatrix} \begin{pmatrix} \lambda_q \\ \theta_q \end{pmatrix}, \tag{A6}$$

where $\mathcal{M}^{q,E}_{11} = (\mathcal{M}^q_{11} + \mathcal{M}^q_{22})/2$ is an even function of $i\nu_n$ and $\mathcal{M}^{q,O}_{11} = (\mathcal{M}^q_{11} - \mathcal{M}^q_{22})/2$ is an odd one. In particular, when $q \to q_0 = (\mathbf{0}, 0)$, since the off-diagonal terms $\mathcal{M}^{q_0,O}_{11} = 0$ necessarily vanish, we observe that the amplitude and phase modes are always decoupled in the low-momentum and low-frequency limit. Furthermore, the fact that $\mathcal{M}^{q_0,E}_{11} - \mathcal{M}^{q_0}_{12} = 0$ vanish due to the saddle-point condition [i.e., the order parameter Eq. (10)] suggests that the low-frequency phase mode is always gapless, and we identify it as the Goldstone mode. Similarly, when $q \to q_I = (\mathbf{0}, 2\Delta_0)$, the fact that $\mathcal{M}^{q_I,E}_{11} + \mathcal{M}^{q_I}_{12} = 0$ vanish, due again to the saddle-point condition, suggests that the amplitude mode is gapped with $2\Delta_0$, and we identify it as the Higgs mode. Note that since $\mathcal{M}^{q_I,O}_{11}$ does not vanish in general, the latter statement is strictly valid only in the BCS limit where $\mathcal{M}^{q_I,O}_{11}$ is small and negligible.

Given that the terms with the prefactor $(f-f')$ have the usual Landau singularity for the $q \to (\mathbf{0}, 0)$ limit and causes the collective modes to decay, a small-$q$ expansion is well defined only in two cases: (i) just below $T_c$, as discussed in Ref. [44], and (ii) at $T = 0$, which is discussed in the main text.

## APPENDIX B: NUMERICAL IMPLEMENTATION

To verify the accuracy of our numerical results, we conducted calculations using two independent numerical implementations. In the first approach, we computed **k**-space sums by dividing the BZ into approximately $10^6$ unit cells. In the second method, we converted **k**-space sums into **k**-space integrals through $\sum_{\mathbf{k}} \to \frac{\mathcal{V}}{8\pi^3}\int d^3\mathbf{k}$ and evaluated them using the adaptive CUBPACK integration library [56]. Although both implementations yielded identical results, the second method significantly speeds up the calculations. Additionally, for any given values of $F$ and $U$, we obtained self-consistent solutions for Eqs. (10) and (11) numerically by iterating $\Delta_0$ and $\mu$ through a hybrid root-finding algorithm of MINPACK that combines the bisection and secant methods. In particular, for generating the colored maps of various physical observables in the main text, we scanned the $(F, U)$ plane using a $400 \times 400$ mesh, resulting in approximately 160 000 repetitions of the iterative approach. Such a dense mesh was necessary to reveal the density of states (DOS) features on the periphery of the white regions including the flat bands at $\mu = -2t$, van Hove singularities at $\mu = \{0, 4t\}$ or, equivalently, at $F \approx \{1.19, 1.81\}$, and the critical semimetal point at $\mu = 2t$ or, equivalently, at $F = 3/2$. While the iterative approach efficiently converged over a wide range of parameters, we encountered convergence issues only in the BCS regime when $\Delta_0/t \ll 1$. We emphasize that it is possible to address such convergence problems on demand, i.e., for any desired $F$ value, by providing more accurate input parameters for $\Delta_0$ and $\mu$ for the initial iteration. However, automating such fine-tuning operations proved to be difficult for the entire regime of interest in this paper.


[1] J. P. Provost and G. Vallee, Riemannian structure on manifolds of quantum states, Commun. Math. Phys. **76**, 289 (1980).

[2] M. V. Berry, Quantal phase factors accompanying adiabatic changes, Proc. R. Soc. London. A. Math. Phys. Sci. **392**, 45 (1984).

[3] R. Resta, The insulating state of matter: A geometrical theory, Europhys. J. B **79**, 121 (2011).

[4] D. Xiao, M.-C. Chang, and Q. Niu, Berry phase effects on electronic properties, Rev. Mod. Phys. **82**, 1959 (2010).

[5] X.-L. Qi and S.-C. Zhang, Topological insulators and superconductors, Rev. Mod. Phys. **83**, 1057 (2011).

[6] C.-K. Chiu, J. C. Y. Teo, A. P. Schnyder, and S. Ryu, Classification of topological quantum matter with symmetries, Rev. Mod. Phys. **88**, 035005 (2016).

[7] A. Bansil, H. Lin, and T. Das, Colloquium: Topological band theory, Rev. Mod. Phys. **88**, 021004 (2016).

[8] S. Peotta and P. Törmä, Superfluidity in topologically nontrivial flat bands, Nat. Commun. **6**, 8944 (2015).

[9] P. Törmä, S. Peotta, and B. A. Bernevig, Superconductivity, superfluidity and quantum geometry in twisted multilayer systems, Nat. Rev. Phys. **4**, 528 (2022).

[10] K.-E. Huhtinen, J. Herzog-Arbeitman, A. Chew, B. A. Bernevig, and P. Törmä, Revisiting flat band superconductivity: Dependence on minimal quantum metric and band touchings, Phys. Rev. B **106**, 014518 (2022).

[11] P. Törmä, Essay: Where can quantum geometry lead us? Phys. Rev. Lett. **131**, 240001 (2023).

[12] X. Hu, T. Hyart, D. I. Pikulin, and E. Rossi, Geometric and conventional contribution to the superfluid weight in twisted bilayer graphene, Phys. Rev. Lett. **123**, 237002 (2019).

[13] J. Herzog-Arbeitman, V. Peri, F. Schindler, S. D. Huber, and B. A. Bernevig, Superfluid weight bounds from symmetry and quantum geometry in flat bands, Phys. Rev. Lett. **128**, 087002 (2022).

[14] J. S. Hofmann, E. Berg, and D. Chowdhury, Superconductivity, charge density wave, and supersolidity in flat bands with a tunable quantum metric, Phys. Rev. Lett. **130**, 226001 (2023).

[15] V. Khodel and V. Shaginyan, Superfluidity in system with fermion condensate, JETP Lett. **51**, 553 (1990).

[16] N. B. Kopnin, T. T. Heikkilä, and G. E. Volovik, High-temperature surface superconductivity in topological flat-band systems, Phys. Rev. B **83**, 220503(R) (2011).

[17] L. Classen, Geometry rescues superconductivity in twisted graphene, Physics **13**, 23 (2020).

[18] D. J. Scalapino, S. R. White, and S. C. Zhang, Superfluid density and the Drude weight of the Hubbard model, Phys. Rev. Lett. **68**, 2830 (1992).

[19] P. J. H. Denteneer, G. An, and J. M. J. van Leeuwen, Helicity modulus in the two-dimensional Hubbard model, Phys. Rev. B **47**, 6256 (1993).

[20] H. Tajima, Y. Yerin, A. Perali, and P. Pieri, Enhanced critical temperature, pairing fluctuation effects, and BCS-BEC crossover in a two-band Fermi gas, Phys. Rev. B **99**, 180503(R) (2019).

[21] H. Tajima, Y. Yerin, P. Pieri, and A. Perali, Mechanisms of screening or enhancing the pseudogap throughout the two-band Bardeen-Cooper-Schrieffer to Bose-Einstein condensate crossover, Phys. Rev. B **102**, 220504(R) (2020).

[22] A. Julku, S. Peotta, T. I. Vanhala, D.-H. Kim, and P. Törmä, Geometric origin of superfluidity in the Lieb-lattice flat band, Phys. Rev. Lett. **117**, 045303 (2016).

[23] L. Liang, T. I. Vanhala, S. Peotta, T. Siro, A. Harju, and P. Törmä, Band geometry, Berry curvature, and superfluid weight, Phys. Rev. B **95**, 024515 (2017).

[24] M. Iskin, Berezinskii-Kosterlitz-Thouless transition in the time-reversal-symmetric Hofstadter-Hubbard model, Phys. Rev. A **97**, 013618 (2018).

[25] M. Iskin, Origin of flat-band superfluidity on the Mielke checkerboard lattice, Phys. Rev. A **99**, 053608 (2019).

[26] Y.-R. Wu, X.-F. Zhang, C.-F. Liu, W.-M. Liu, and Y.-C. Zhang, Superfluid density and collective modes of fermion superfluid in dice lattice, Sci. Rep. **11**, 13572 (2021).

[27] S. M. Chan, B. Grémaud, and G. G. Batrouni, Pairing and superconductivity in quasi-one-dimensional flat-band systems: Creutz and sawtooth lattices, Phys. Rev. B **105**, 024502 (2022).

[28] S. M. Chan, B. Grémaud, and G. G. Batrouni, Designer flat bands: Topology and enhancement of superconductivity, Phys. Rev. B **106**, 104514 (2022).

[29] T. Kitamura, T. Yamashita, J. Ishizuka, A. Daido, and Y. Yanase, Superconductivity in monolayer FeSe enhanced by quantum geometry, Phys. Rev. Res. **4**, 023232 (2022).
[30] D. Porlles and W. Chen, Quantum geometry of singlet superconductors, Phys. Rev. B **108**, 094508 (2023).
[31] S. A. Chen and K. T. Law, Ginzburg-Landau theory of flat-band superconductors with quantum metric, Phys. Rev. Lett. **132**, 026002 (2024).
[32] G. Jiang and Y. Barlas, Pair density waves from local band geometry, Phys. Rev. Lett. **131**, 016002 (2023).
[33] J.-X. Hu, S. A. Chen, and K. Law, Anomalous coherence length in superconductors with quantum metric, arXiv:2308.05686
[34] J. S. Gardner, M. J. P. Gingras, and J. E. Greedan, Magnetic pyrochlore oxides, Rev. Mod. Phys. **82**, 53 (2010).
[35] J. P. Wakefield, M. Kang, P. M. Neves, D. Oh, S. Fang, R. McTigue, S. Frank Zhao, T. N. Lamichhane, A. Chen, S. Lee *et al.*, Three-dimensional flat bands in pyrochlore metal CaNi2, Nature (London) **623**, 301 (2023).
[36] J. Huang, C. Setty, L. Deng, J.-Y. You, H. Liu, S. Shao, J. S. Oh, Y. Guo, Y. Zhang, Z. Yue *et al.*, Observation of flat bands and Dirac cones in a pyrochlore lattice superconductor, arXiv:2304.09066.
[37] H.-M. Guo and M. Franz, Three-dimensional topological insulators on the pyrochlore lattice, Phys. Rev. Lett. **103**, 206805 (2009).
[38] T. Mizoguchi and M. Udagawa, Flat-band engineering in tight-binding models: Beyond the nearest-neighbor hopping, Phys. Rev. B **99**, 235118 (2019).
[39] M. Iskin, Effective-mass tensor of the two-body bound states and the quantum-metric tensor of the underlying Bloch states in multiband lattices, Phys. Rev. A **105**, 023312 (2022).
[40] M. Iskin, Variational approach for the two-body problem in a multiband extended-Hubbard model, arXiv:2404.01117.
[41] A. Leggett, *Quantum Liquids: Bose Condensation and Cooper Pairing in Condensed-matter Systems* (Oxford University Press, UK, 2008).
[42] A. Daido, T. Kitamura, and Y. Yanase, Quantum geometry encoded to pair potentials, arXiv:2310.15558.
[43] A. L. Fetter and J. D. Walecka, *Quantum Theory of Many-Particle Systems* (McGraw-Hill, Boston, 1971).
[44] M. Iskin, Extracting quantum-geometric effects from Ginzburg-Landau theory in a multiband Hubbard model, Phys. Rev. B **107**, 224505 (2023).
[45] H. Tian, X. Gao, Y. Zhang, S. Che, T. Xu, P. Cheung, K. Watanabe, T. Taniguchi, M. Randeria, F. Zhang *et al.*, Evidence for Dirac flat band superconductivity enabled by quantum geometry, Nature (London) **614**, 440 (2023).
[46] P. Noziöres and S. Schmitt-Rink, Bose condensation in an attractive fermion gas: From weak to strong coupling superconductivity, J. Low Temp. Phys. **59**, 195 (1985).
[47] C. A. R. Sá de Melo, M. Randeria, and J. R. Engelbrecht, Crossover from BCS to Bose superconductivity: Transition temperature and time-dependent Ginzburg-Landau theory, Phys. Rev. Lett. **71**, 3202 (1993).
[48] M. Iskin, Collective excitations of a BCS superfluid in the presence of two sublattices, Phys. Rev. A **101**, 053631 (2020).
[49] J. R. Engelbrecht, M. Randeria, and C. A. R. Sáde Melo, BCS to Bose crossover: Broken-symmetry state, Phys. Rev. B **55**, 15153 (1997).
[50] In the case of two-band lattices, our expansion coefficients recover all of the previous results, except for the first line of Eq. (28) which is missing there [48].
[51] V. M. Loktev, R. M. Quick, and S. G. Sharapov, Phase fluctuations and pseudogap phenomena, Phys. Rep. **349**, 1 (2001).
[52] E. Taylor, A. Griffin, N. Fukushima, and Y. Ohashi, Pairing fluctuations and the superfluid density through the BCS-BEC crossover, Phys. Rev. A **74**, 063626 (2006).
[53] M. Iskin, Hofstadter-Hubbard model with opposite magnetic fields: Bardeen-Cooper-Schrieffer pairing and superfluidity in the nearly flat butterfly bands, Phys. Rev. A **96**, 043628 (2017).
[54] M. Iskin and C. A. R. Sá de Melo, Quantum phases of Fermi-Fermi mixtures in optical lattices, Phys. Rev. A **78**, 013607 (2008).
[55] A. M. Rey, K. Burnett, R. Roth, M. Edwards, C. J. Williams, and C. W. Clark, Bogoliubov approach to superfluidity of atoms in an optical lattice, J. Phys. B: At. Mol. Opt. Phys. **36**, 825 (2003).
[56] CUBPACK - Adaptive cubature for simplices, https://people.math.sc.edu/Burkardt/f_src/cubpack/cubpack.html.